MDPI remote sensing

Supplementary Materials for

Deep clouds on Jupiter

Michael H. Wong (UC Berkeley + SETI Inst.),
Gordon L. Bjoraker (NASA Goddard Space Flight Center),
Charles Goullaud (UC Berkeley),
Andrew W. Stephens (Gemini Observatory, NSF's NOIRLab),
Statia Luszcz-Cook (Columbia Univ. + American Museum of Natural History),
Sushil K. Atreya (Univ. Michigan, Ann Arbor),
Imke de Pater (UC Berkeley), and
Shannon Brown (NASA/Caltech Jet Propulsion Laboratory)

Introduction

This Supplementary Materials file provides additional figures not included in the text for brevity. Figures S01-S12 are enlargements and different versions of the data presented in Fig. 1. Table S1 provides additional notes and discussion of individual features identified in Figs. S02, S04, S06, and S08.

Figures S13-S22 show additional output from the radiative transfer modeling. Figures S13-S17 are center-to-limb plots of I/F vs. μ_0, while Figs. S18-S22 are center-to-limb plots of the CM7 ratio vs. μ_0.

Enlarged views of Jupiter near PJ 42

Figure 1 in the main paper presents views of Jupiter near Juno perijove 42, which was at 2022-05-23 02:15 UT. In this section we provide enlarged single-panel views, with some features highlighted for additional discussion in Table S1.

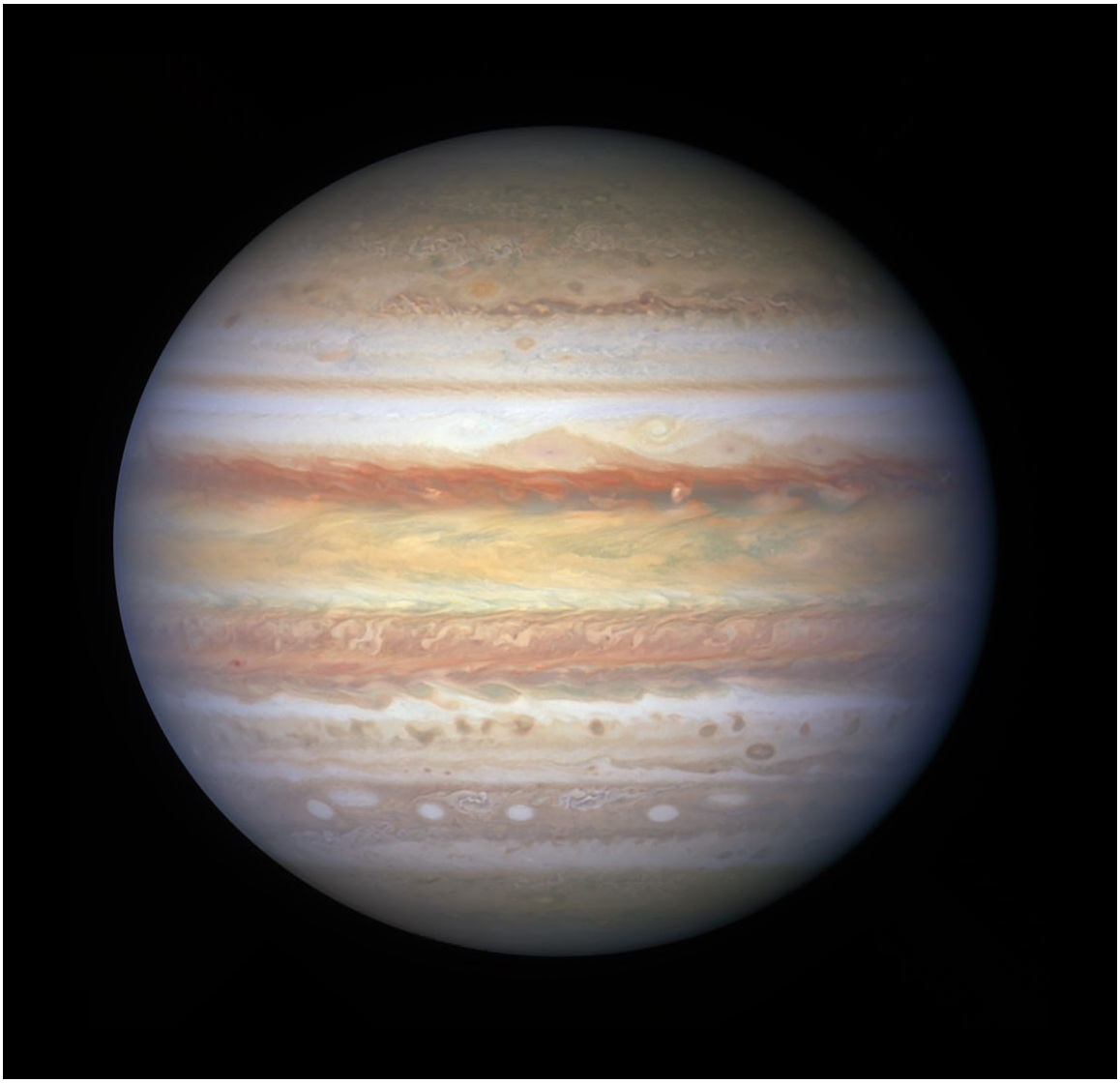

Figure S01. Enlarged view of panel A of Fig. 1 in the main paper: RGB composite.

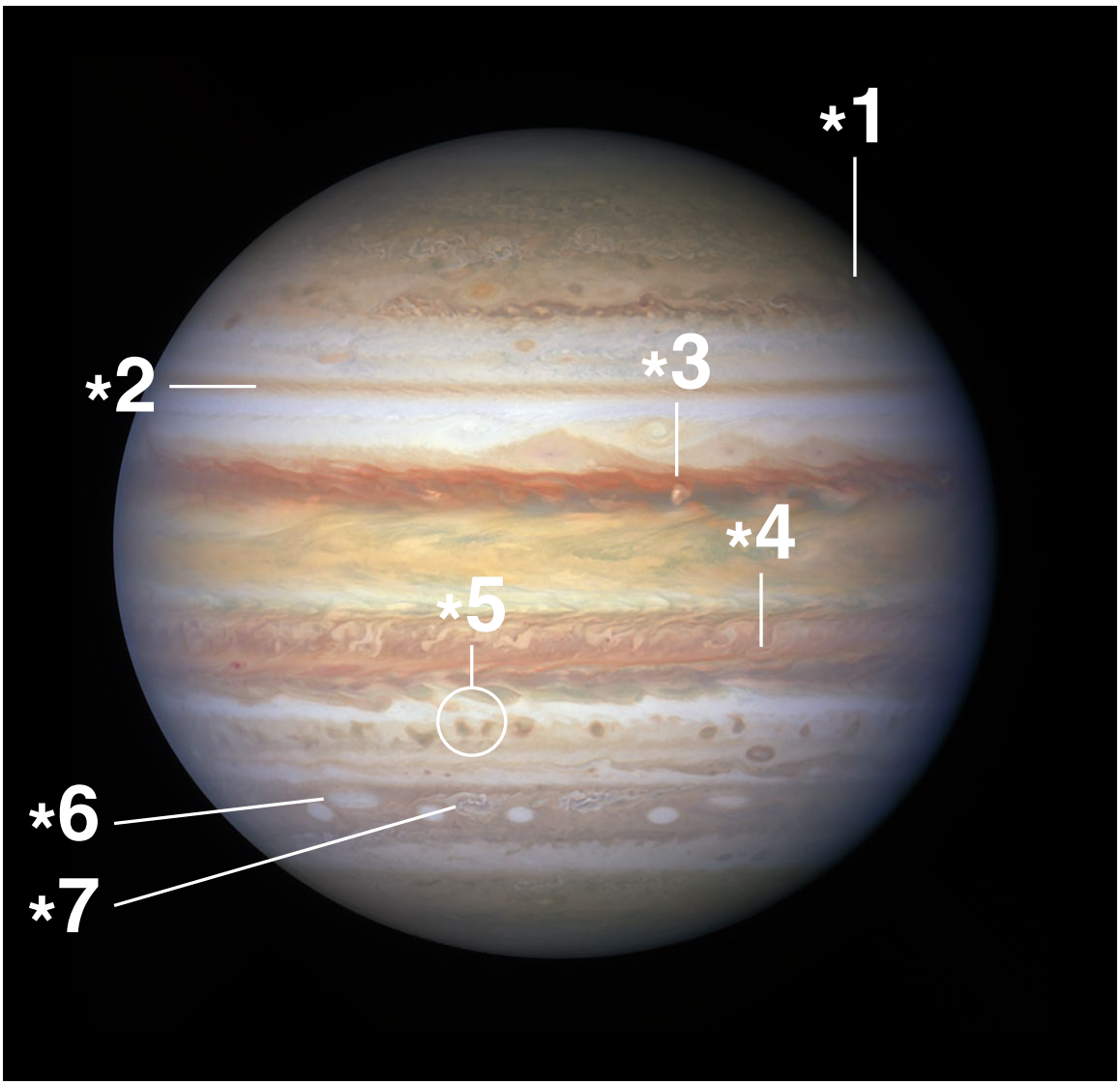

Figure S02. Same as Fig. S01, but with specific features identified for further discussion in Table S1.

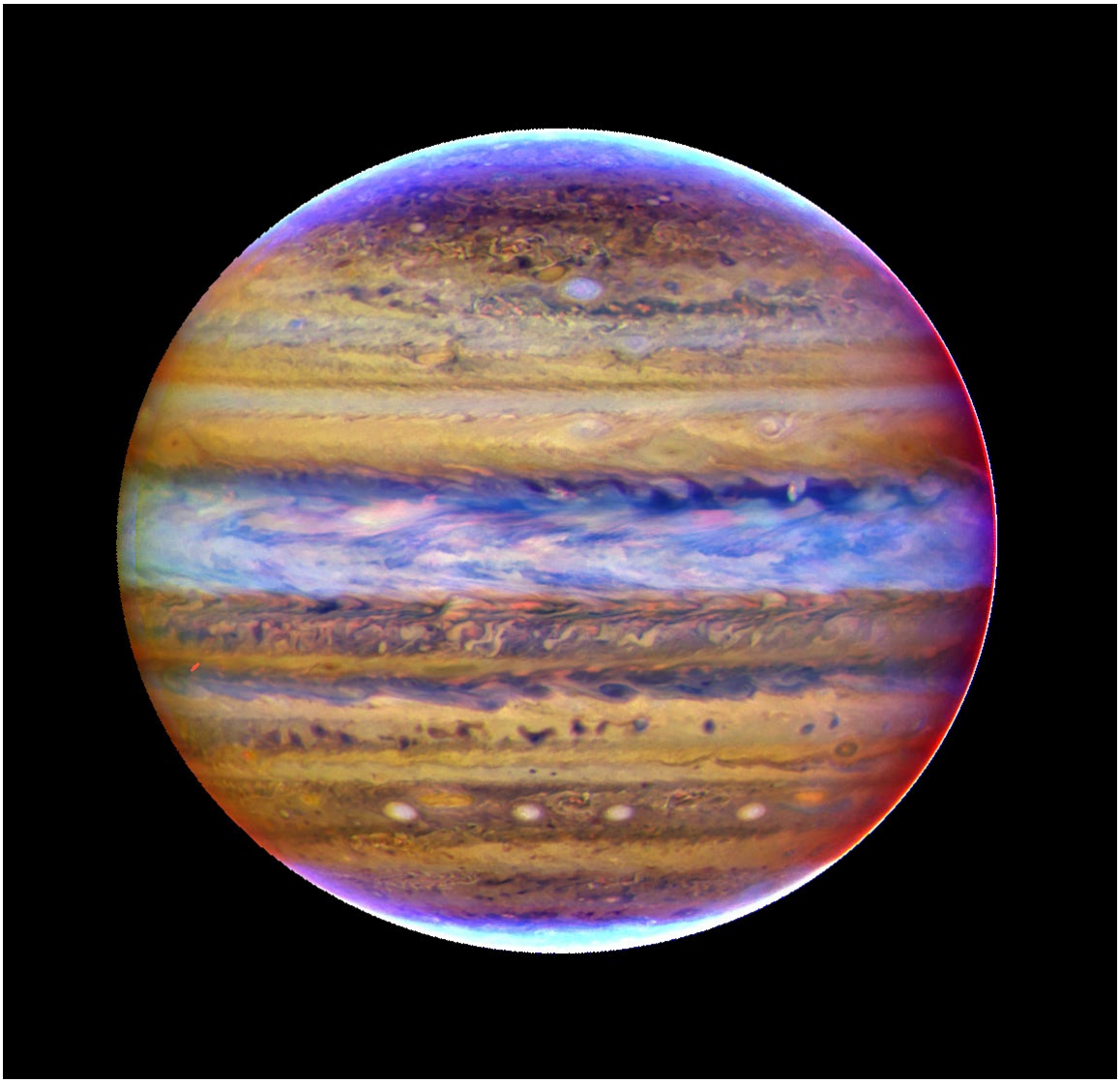

Figure S03. Enlarged view of panel B of Fig. 1 in the main paper: CH_4-band composite. Each channel has been corrected for limb darkening using the Minnaert function.

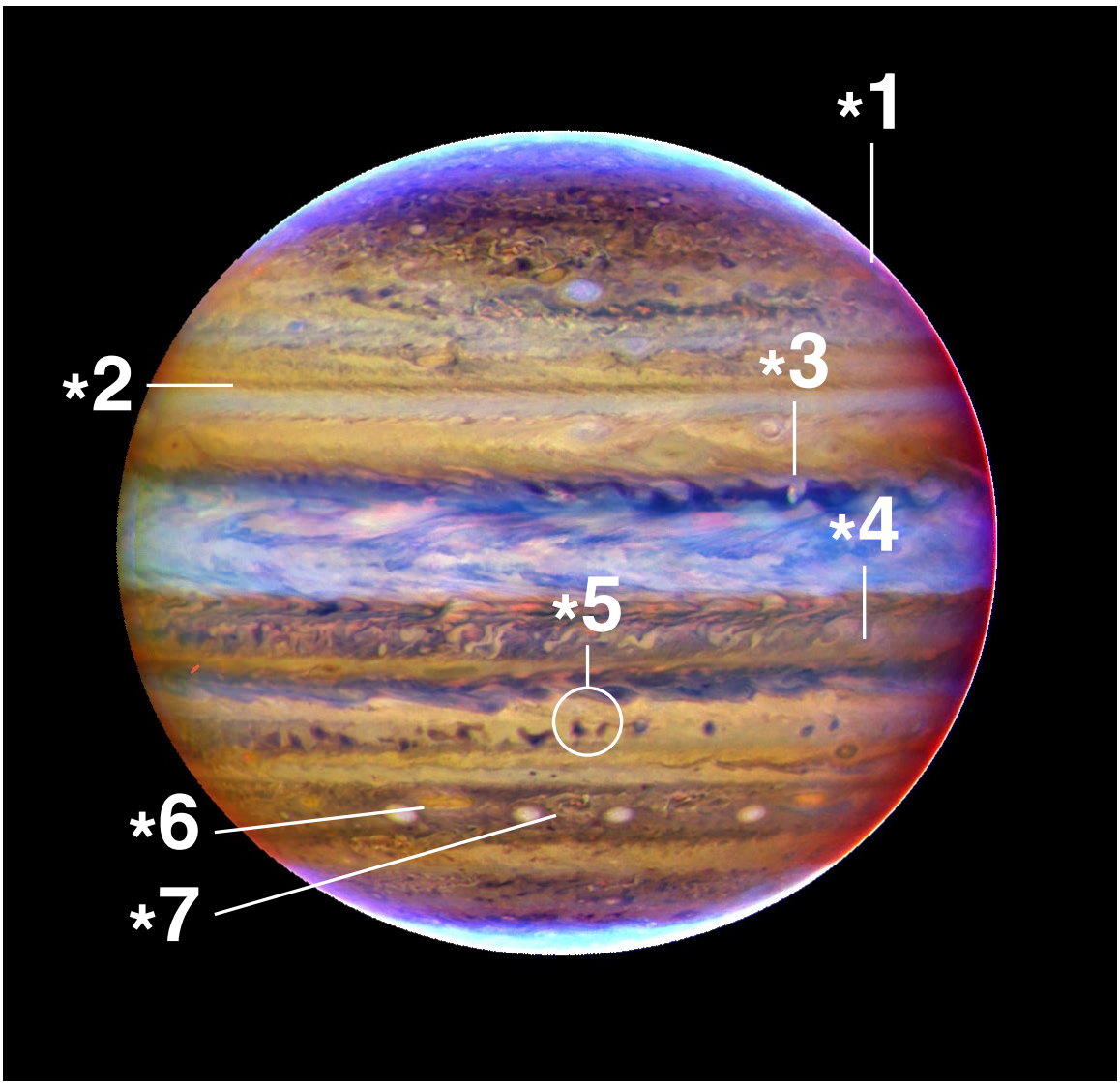

Figure S04. Same as Fig. S03, but with specific features identified for further discussion in Table S1.

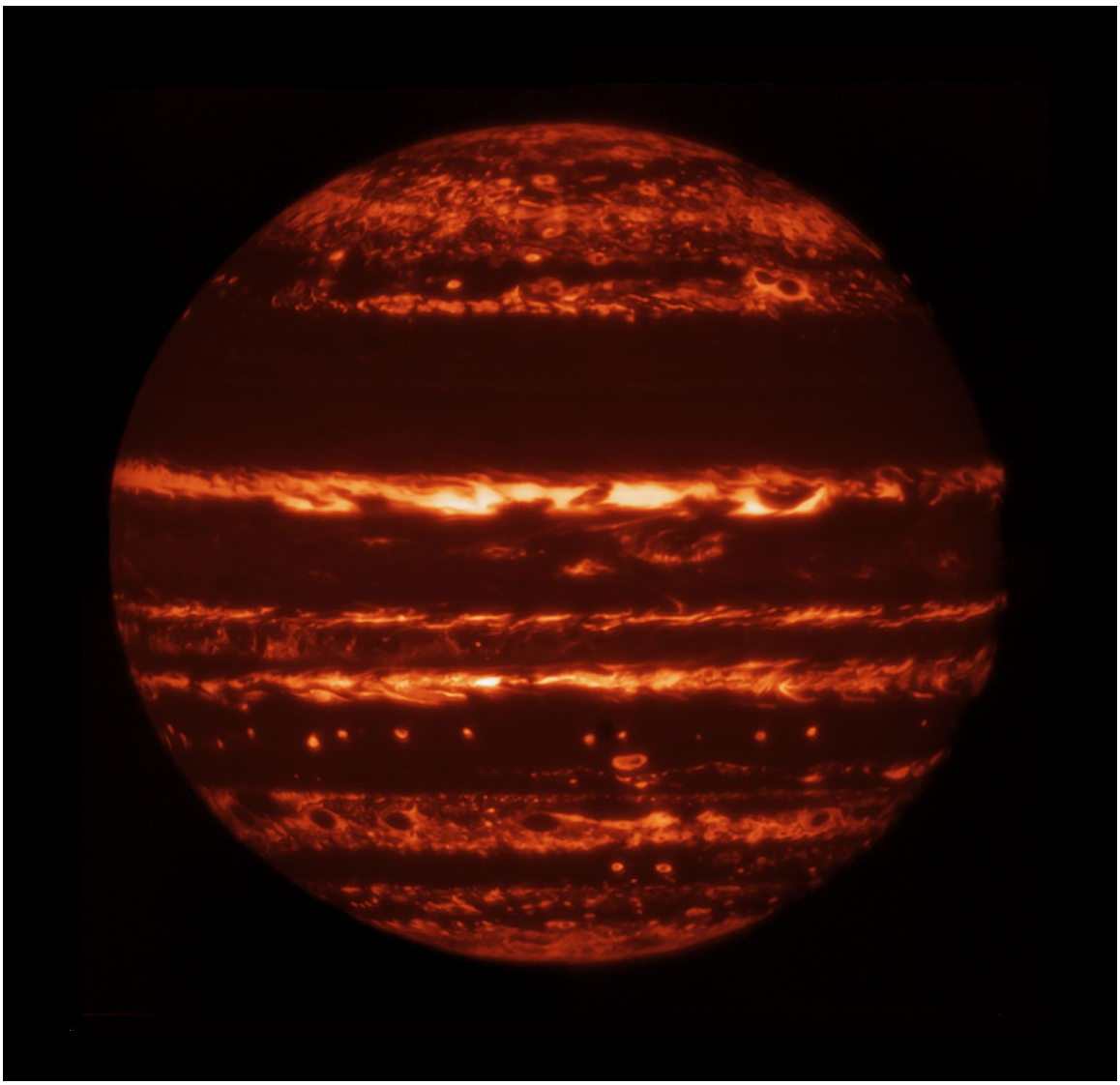

Figure S05. Enlarged view of panel C of Fig. 1 in the main paper: 4.7-μm mosaic. Natural limb darkening is reproduced in the de-rotated full-disk mosaic, and the image is shown scaled with a square-root stretch to increase visual dynamic range and emphasize low-level detail.

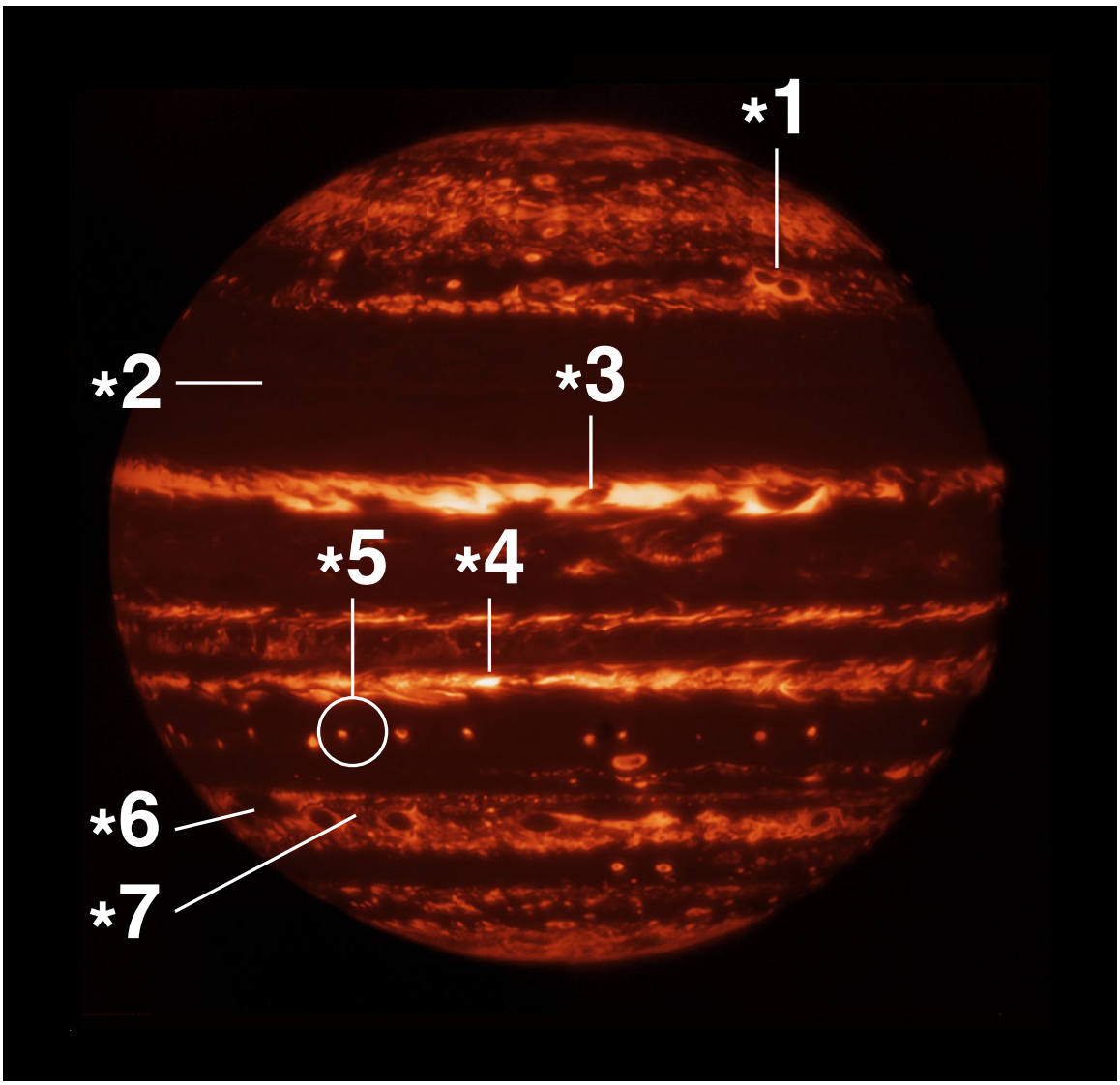

Figure S06. Same as Fig. S05, but with specific features identified for further discussion in Table S1.

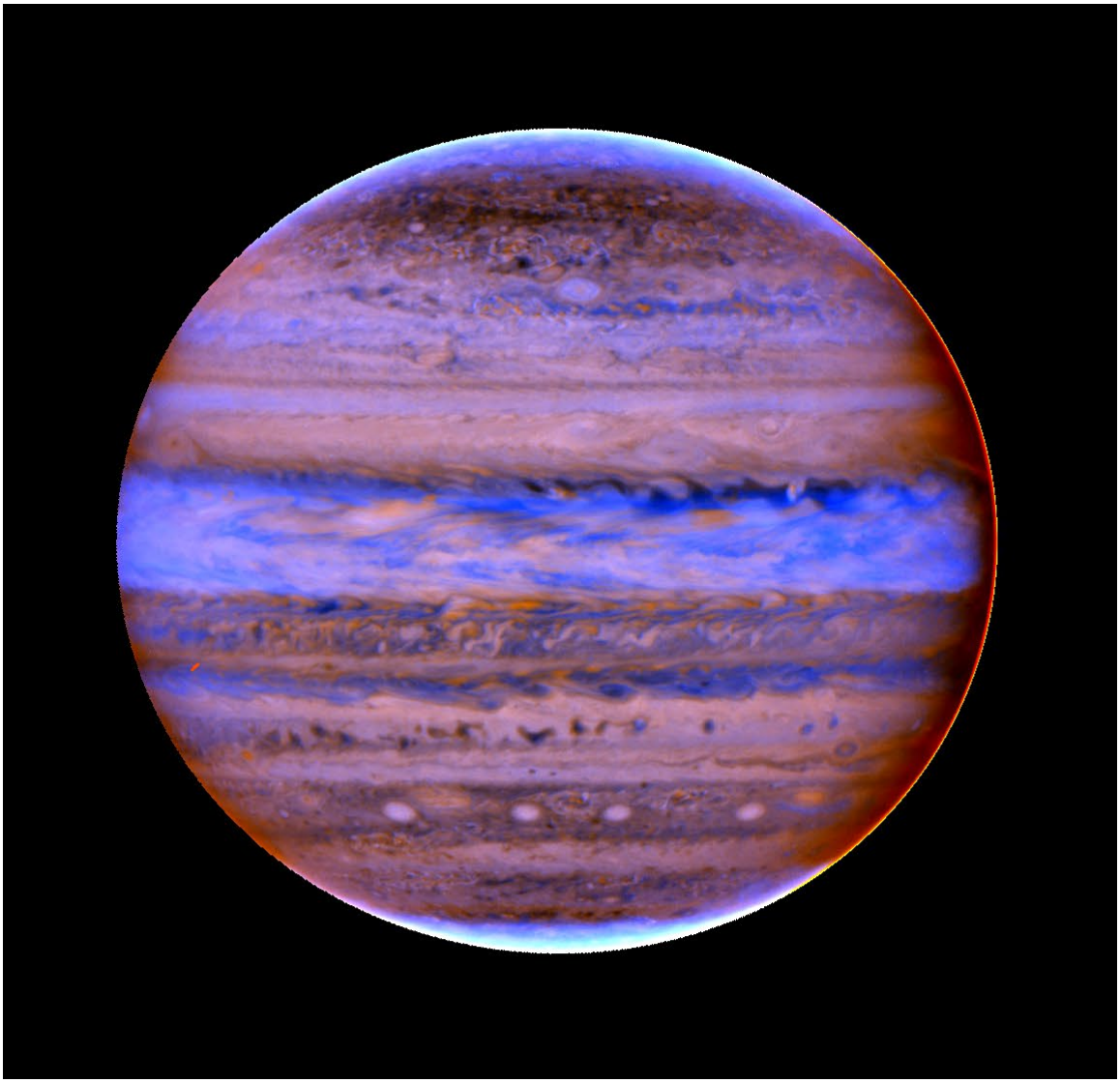

Figure S07. Additional "deep-CH_4" composite not shown in the main paper. The R and G color channels of the composite are the same as for the CH_4-band composite: continuum and 727-nm. The B channel is the ratio of 727-nm to continuum reflectivity (i.e., the inverse of the CM7 ratio). The B channel is bright where upper cloud/haze opacity is high, and dark where more reflectivity comes from deeper layers. This inverse CM7 ratio resembles the strong methane band (Figs. 1F, S11), but probes deeper levels, and like CM7 it is sensitive only to relative depth, not to integrated opacity. The strong visual resemblance between this image and the standard CH_4-band composite (Figs. 1B, S03) indicates that upper tropospheric opacity is the primary control on how deep visible wavelength imaging can see. The upper tropospheric hazes probed at 889 nm are highly correlated with the higher-opacity cloud material in the upper layer, justifying our approach of treating both as a single layer in the radiative transfer model. The R and G channels in the composite are corrected for limb darkening using the Minnaert function, while the B channel is a ratio of data without limb darkening correction.

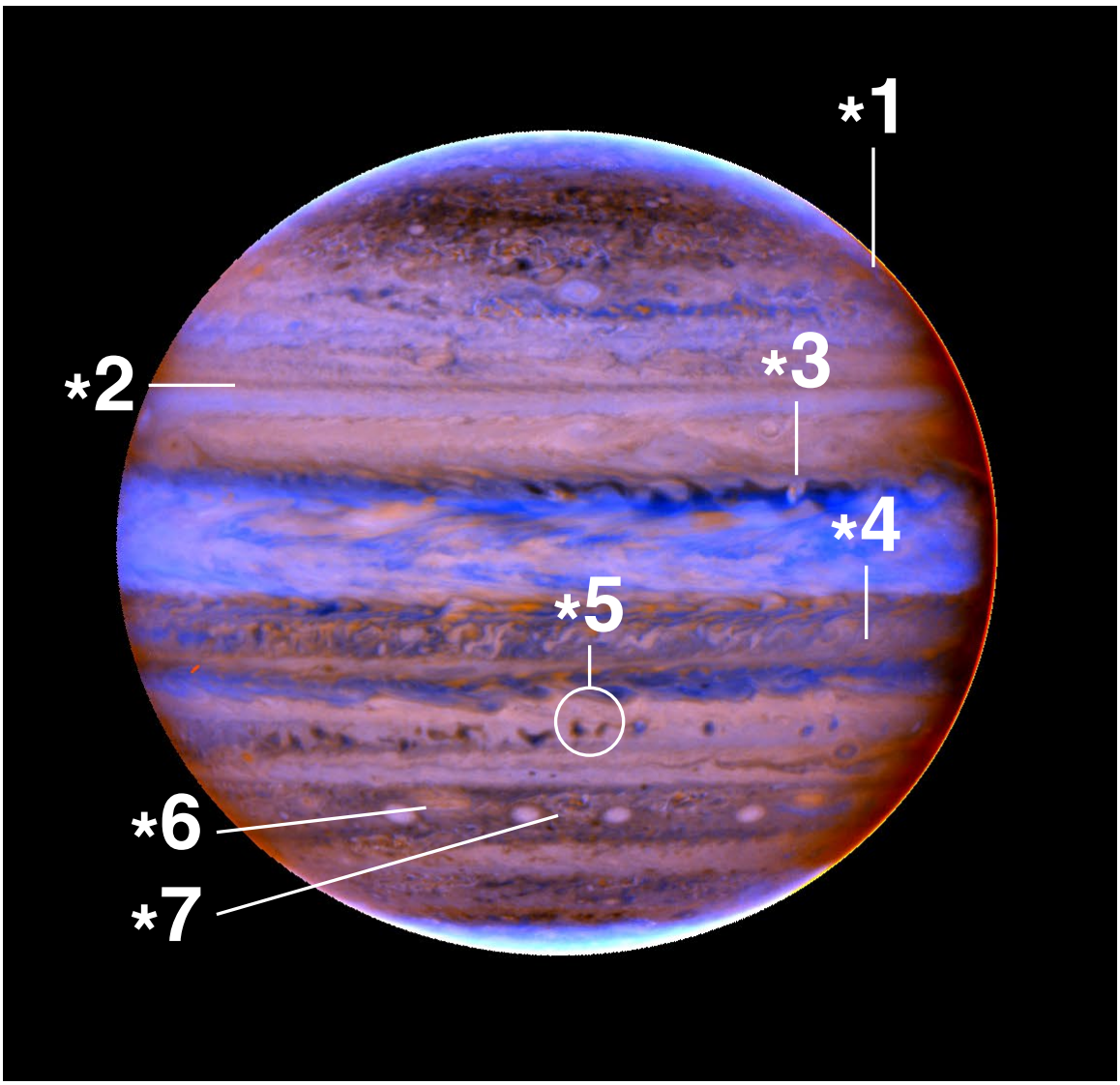

Figure S08. Same as Fig. S07, but with specific features identified for further discussion in Table S1.

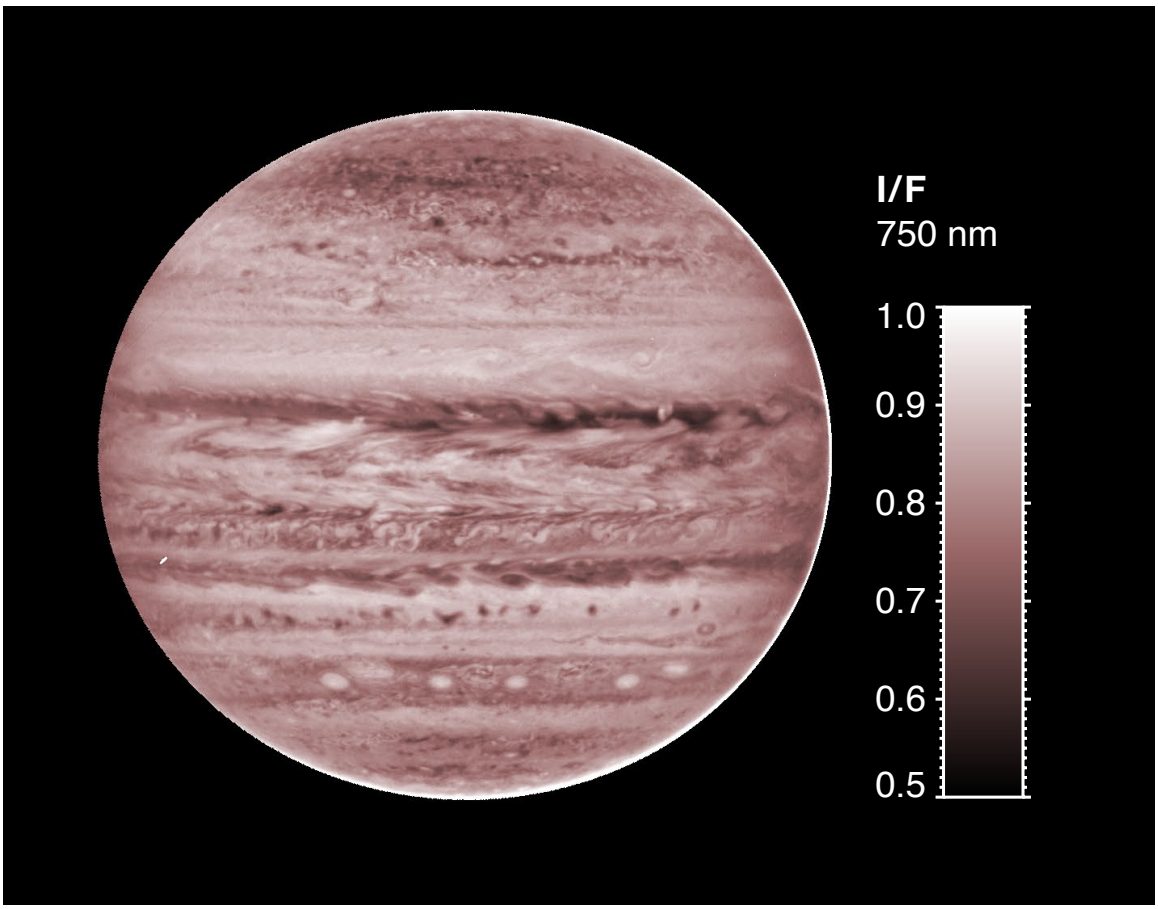

Figure S09. Enlarged view of panel D of Fig. 1 in the main paper: I/F at 750 nm. Image has been corrected for limb darkening using the Minnaert function.

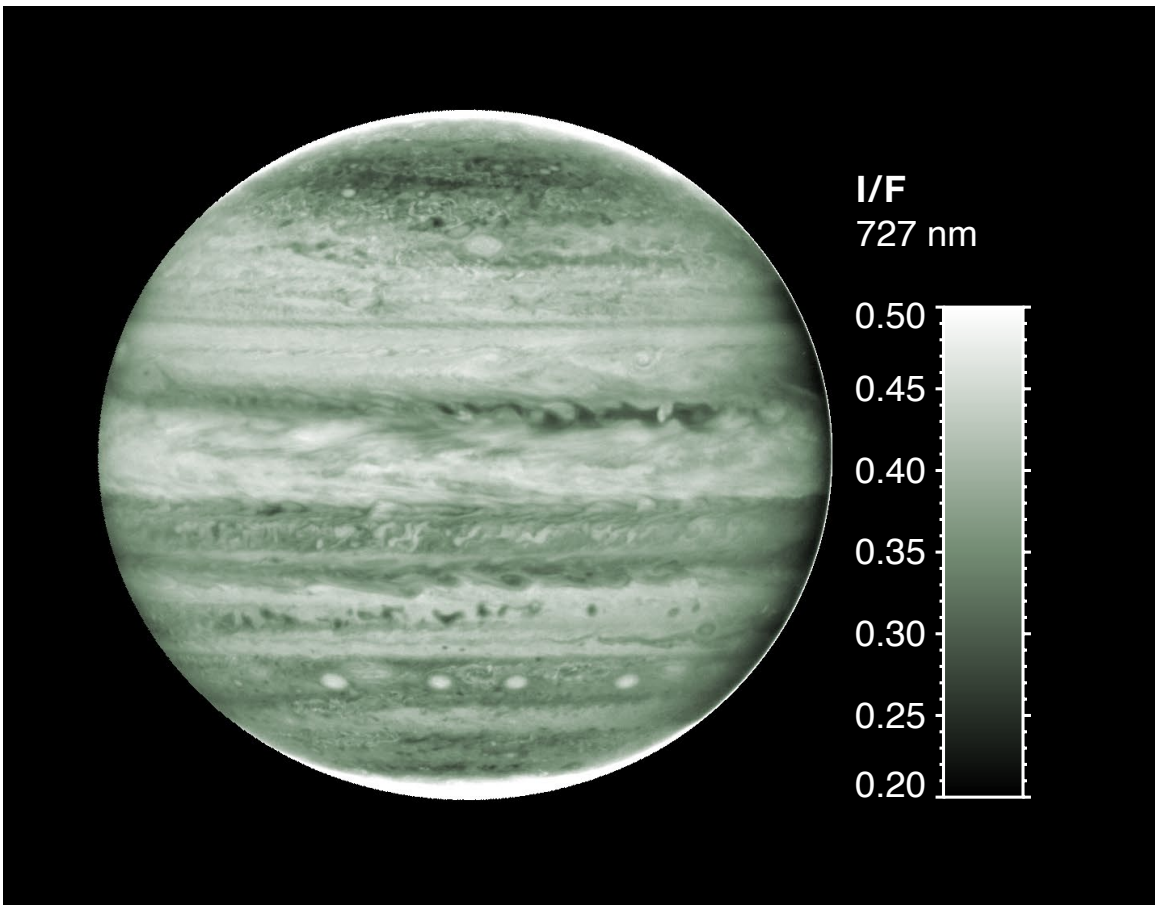

Figure S10. Enlarged view of panel E of Fig. 1 in the main paper: I/F at 727 nm. Image has been corrected for limb darkening using the Minnaert function.

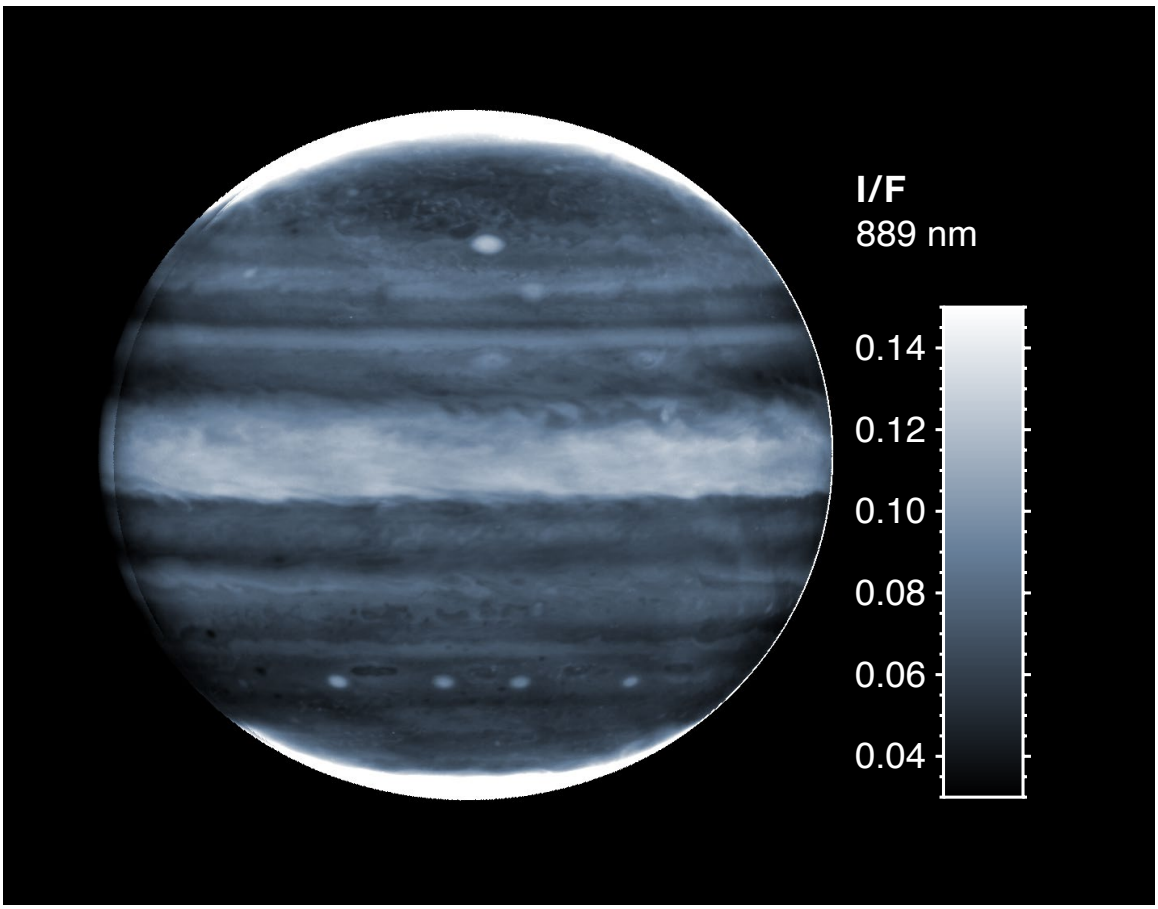

Figure S11. Enlarged view of panel F of Fig. 1 in the main paper: I/F at 889 nm. Image has been corrected for limb darkening using the Minnaert function. An artifact on the west limb is caused because two HST exposures were coadded in the image, and the Minnaert function does not produce a perfect correction for limb darkening, especially at high incidence/emission angles.

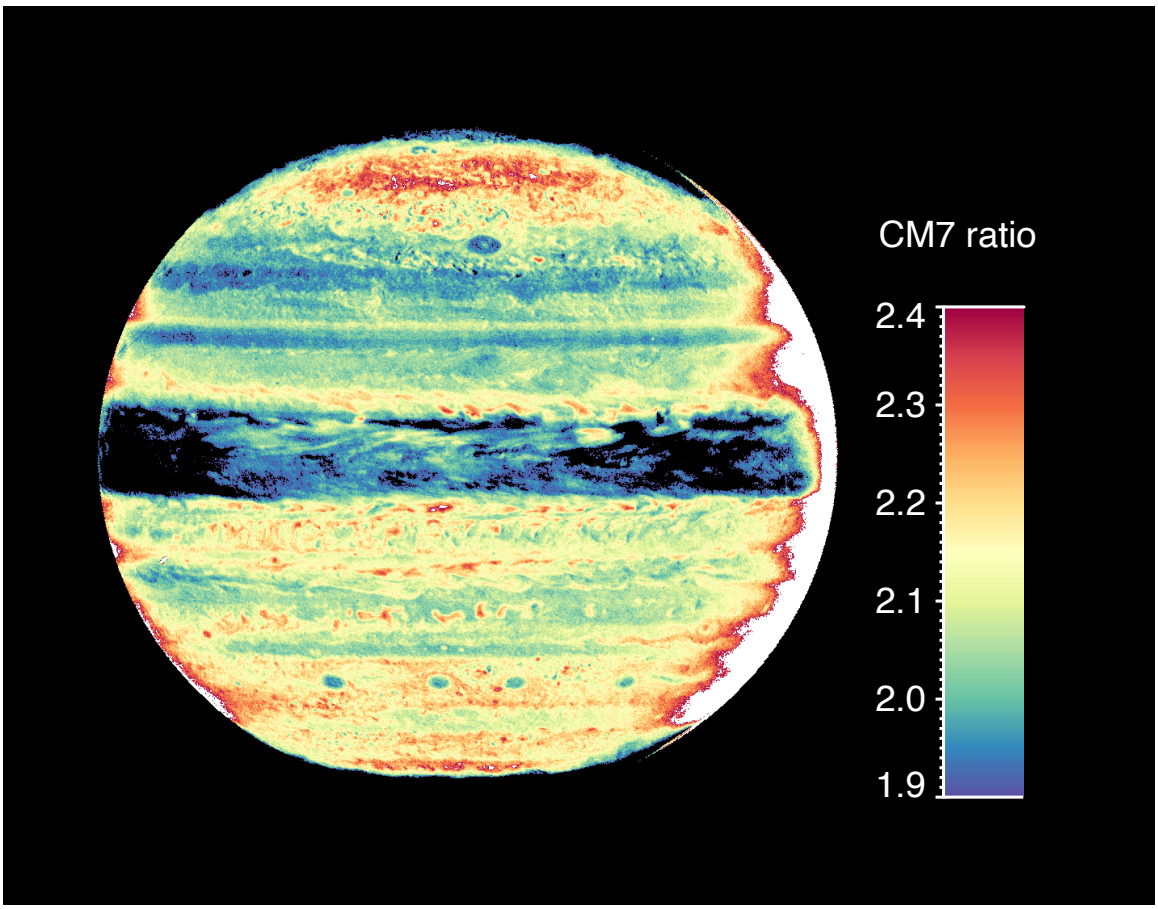

Figure S12. Enlarged view of panel G of Fig. 1 in the main paper: CM7 ratio. The CM7 ratio is based on data without limb darkening correction.

Table S1. Notes on features identified in Figs. S02, S04, S06, S08.

Feature number	Notes
*1	A pair of anticyclones are captured in the process of merging, surrounded by bright 5-μm rings. This event was the 4th merger since 2019 for a vortex identified as NN-WS-6 (Rogers and Mizumoto 2022 [70]).
*2	At 25°N, a visible dark band is also dark in continuum and methane band observations, and the CM7 ratio is locally higher at this latitude. The visible/near-IR data suggest a greater reduction of opacity in the upper cloud/haze level, compared to the deep cloud level. In the thermal infrared, a very faint enhancement in the brightness suggests that the upper-level opacity reduction is not accompanied by a deep opacity reduction (otherwise there would be a brighter feature).
*3	A compact cloud feature located at the special longitude of the "stealth superstorm:" In 2021 and 2022, an unusual condition developed in the North Equatorial Belt. The normal case—with convective plumes occurring randomly distributed in longitude—changed so that convective plumes erupted only at a single active longitude that drifted around the planet near 9°N. Juno observations of a different individual storm plume at this active longitude six months prior detected lightning (Brueshaber et al. 2022 [71]).
*4	The single brightest feature in the 4.7 μm image (panel E). The low deep cloud opacity implied by the brightness enhancement at 4.7-μm is not supported by the HST CH_4-band data: at the location of this feature in the CM7 map, the reflectivity ratio is similar to that of the surrounding areas, suggesting moderately high opacity in the upper cloud/haze layers. We note that ~2 days separate the Gemini and HST observations.
*5	A string of compact dark features spreads over a significant fraction of the disk near 25°S. The features uniformly have high CM7 values, suggesting low upper cloud opacity, and all but one are bright at 4.7 μm, suggesting that deep cloud opacity is also reduced in this string of features. But within the circled region, a pair of similar dark features can be seen in the HST data, with only the darker of the pair showing up in the thermal emission image. It is not clear how cloud opacity could block upwelling thermal radiation, but not reflect sunlight, unless the feature evolved rapidly over the two days separating Gemini and HST observations.
*6,*7	Two cyclonic vortices appear very different in both thermal emission and reflected sunlight. Feature *6 has a uniformly bright appearance and is dark at 5 μm. Feature *7 has a turbulent filamentary appearance. Cyclones are known to cycle between these states (Dowling1995, Iñurrigarro et al. 2020, Hueso et al. 2022 [75–77]).

Additional radiative transfer model output

Figures 12 and 15 show plots of I/F in our deep clouds filters (631 nm, 727 nm, 750 nm) as a function of solar incidence angle cosine μ_0, but only for select model parameters. In Figs. S13-S17, we show outputs from all model runs, providing full coverage of the parameter space tested (see Table 2. In Figs. S18-S22, we show plots of CM7 vs μ_0 for all model cases, supplementing data already shown for select model cases in Figs. 14 and 15.

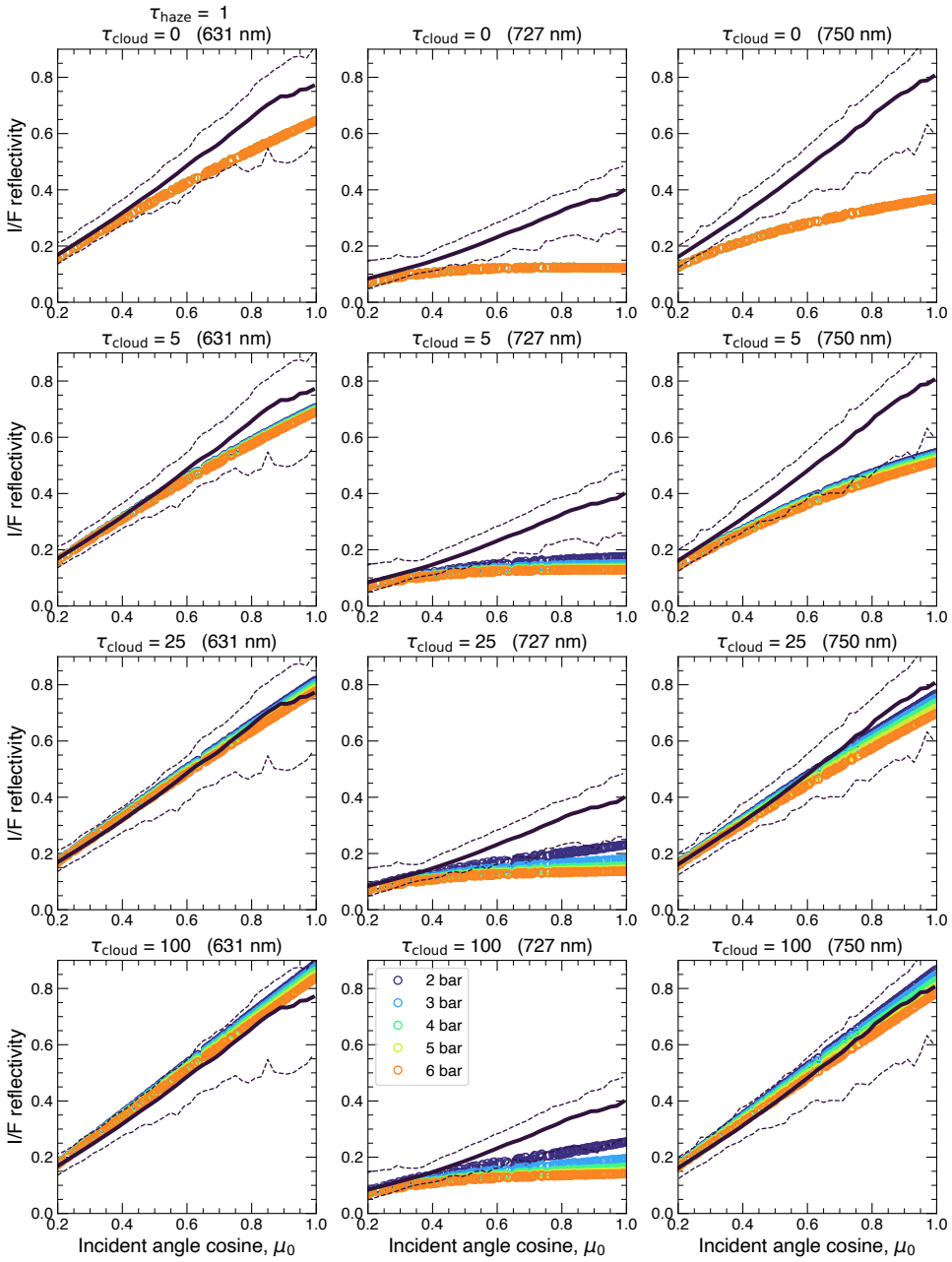

Figure S13. Comparison between observed I/F in 727-nm and continuum filters and modeled center-to-limb curves for all model runs with $\tau_{haze} = 1$.

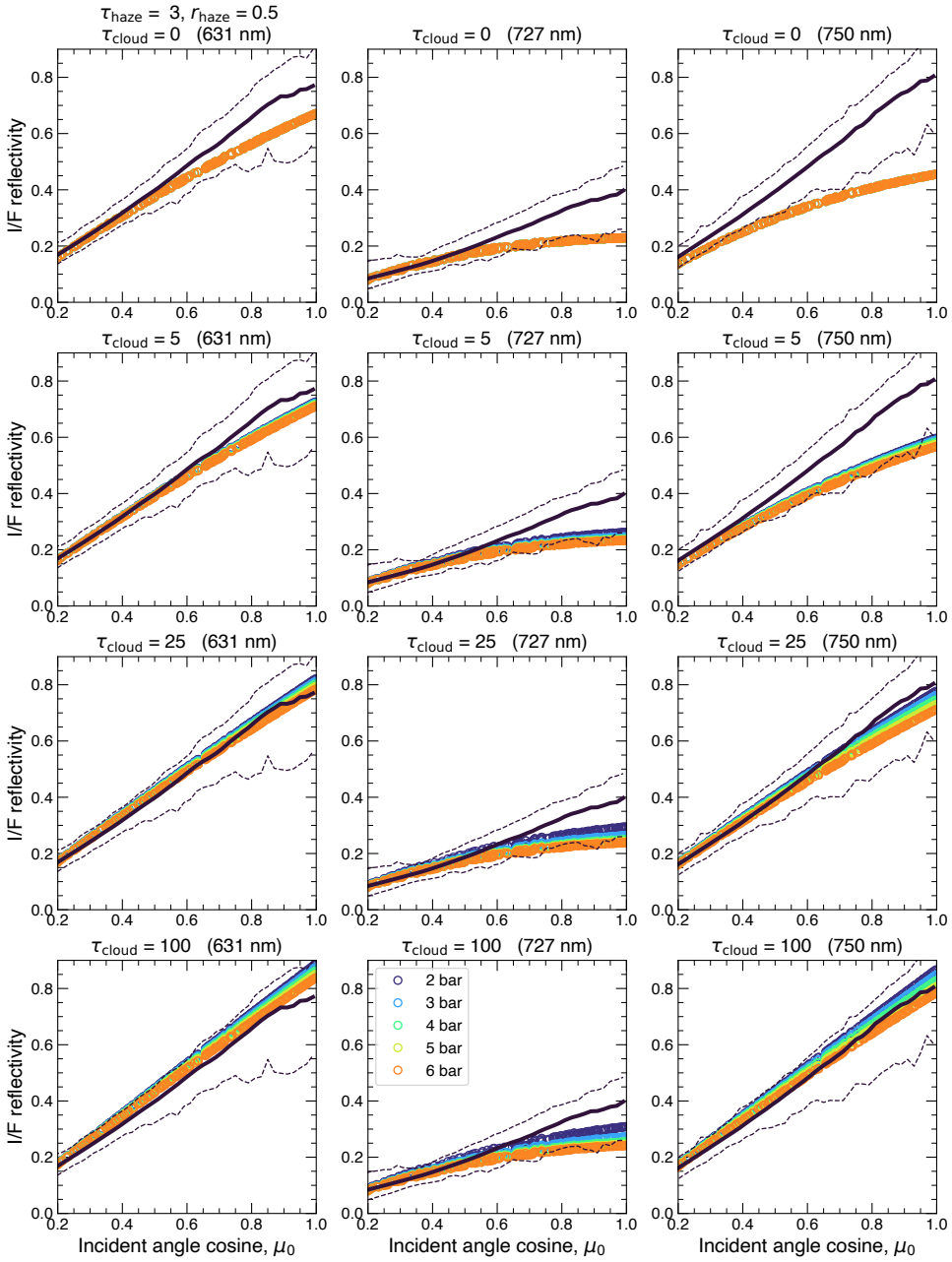

Figure S14. Comparison between observed I/F in 727-nm and continuum filters and modeled center-to-limb curves for all model runs with τ_{haze} = 3.

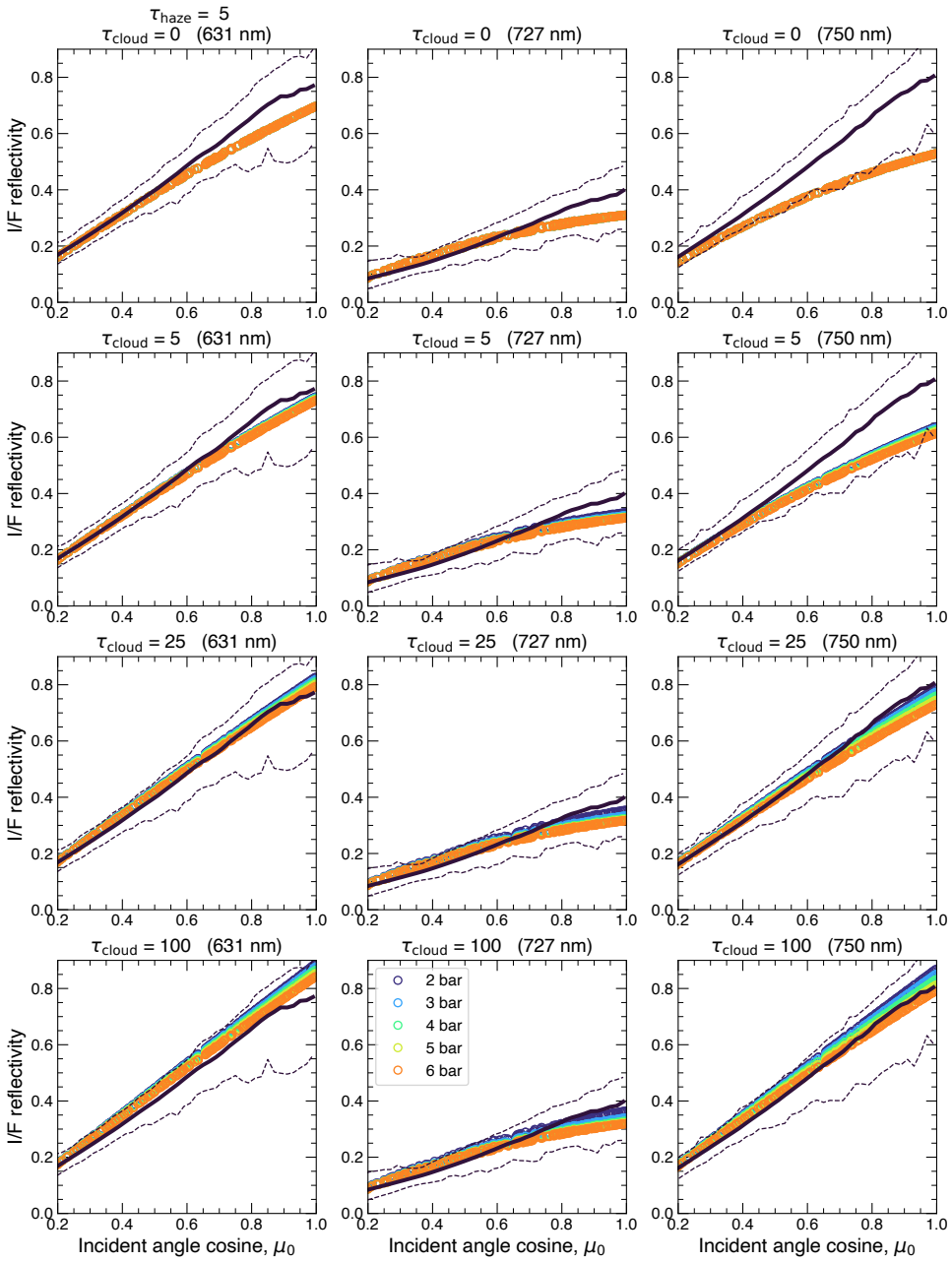

Figure S15. Comparison between observed I/F in 727-nm and continuum filters and modeled center-to-limb curves for all model runs with $\tau_{haze} = 5$.

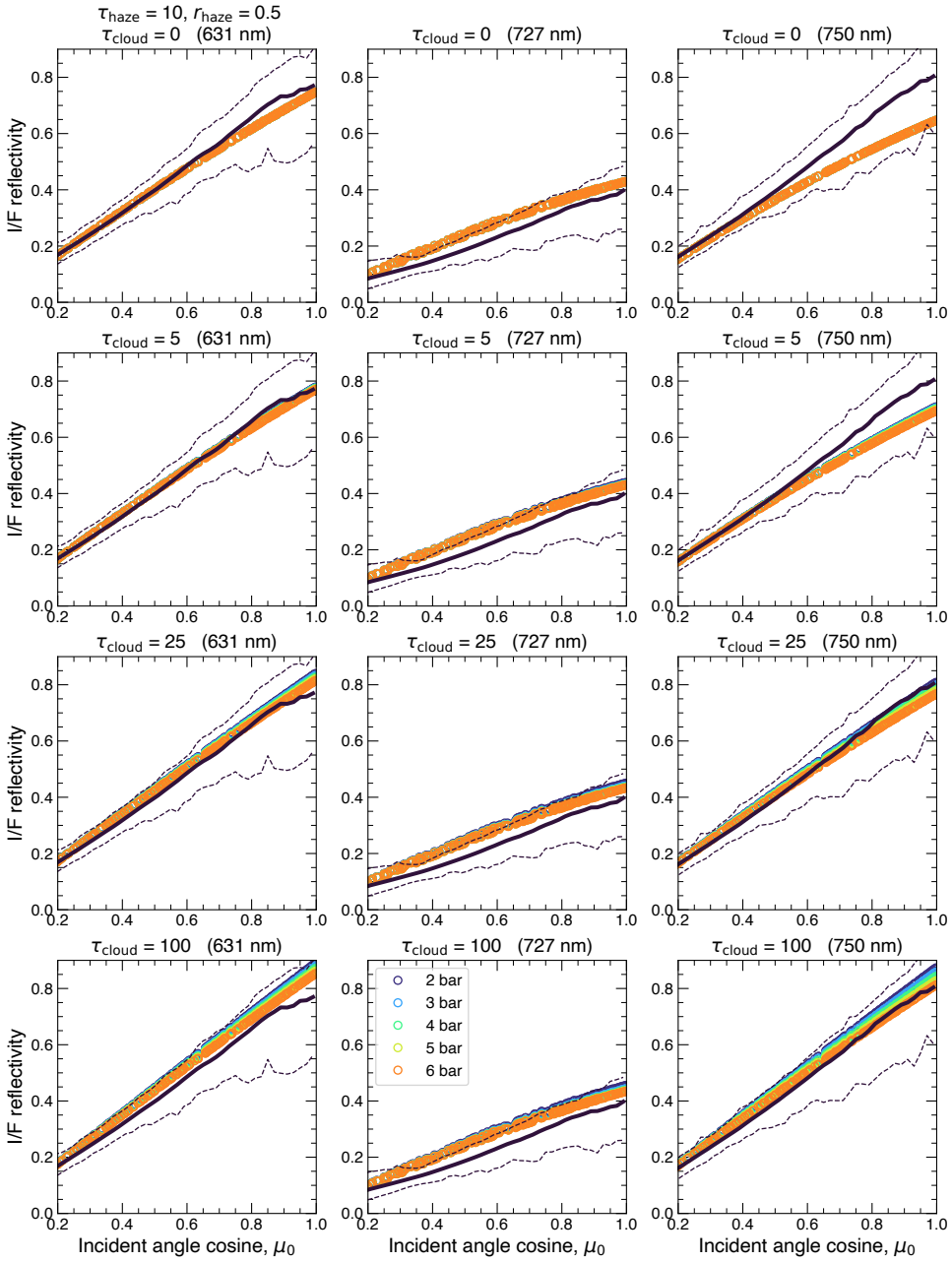

Figure S16. Comparison between observed I/F in 727-nm and continuum filters and modeled center-to-limb curves for all model runs with τ_{haze} = 10.

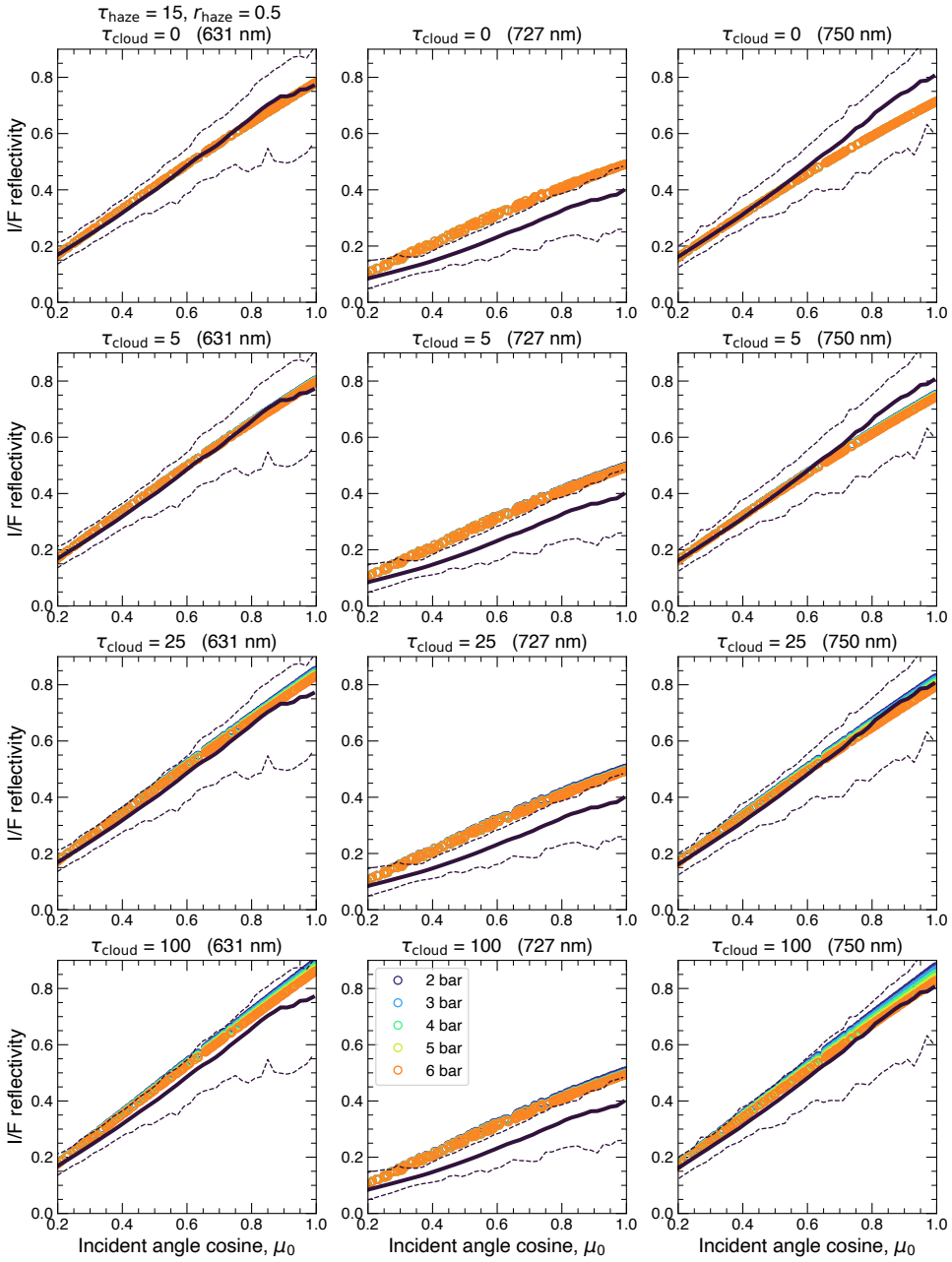

Figure S17. Comparison between observed I/F in 727-nm and continuum filters and modeled center-to-limb curves for all model runs with τ_{haze} = 15.

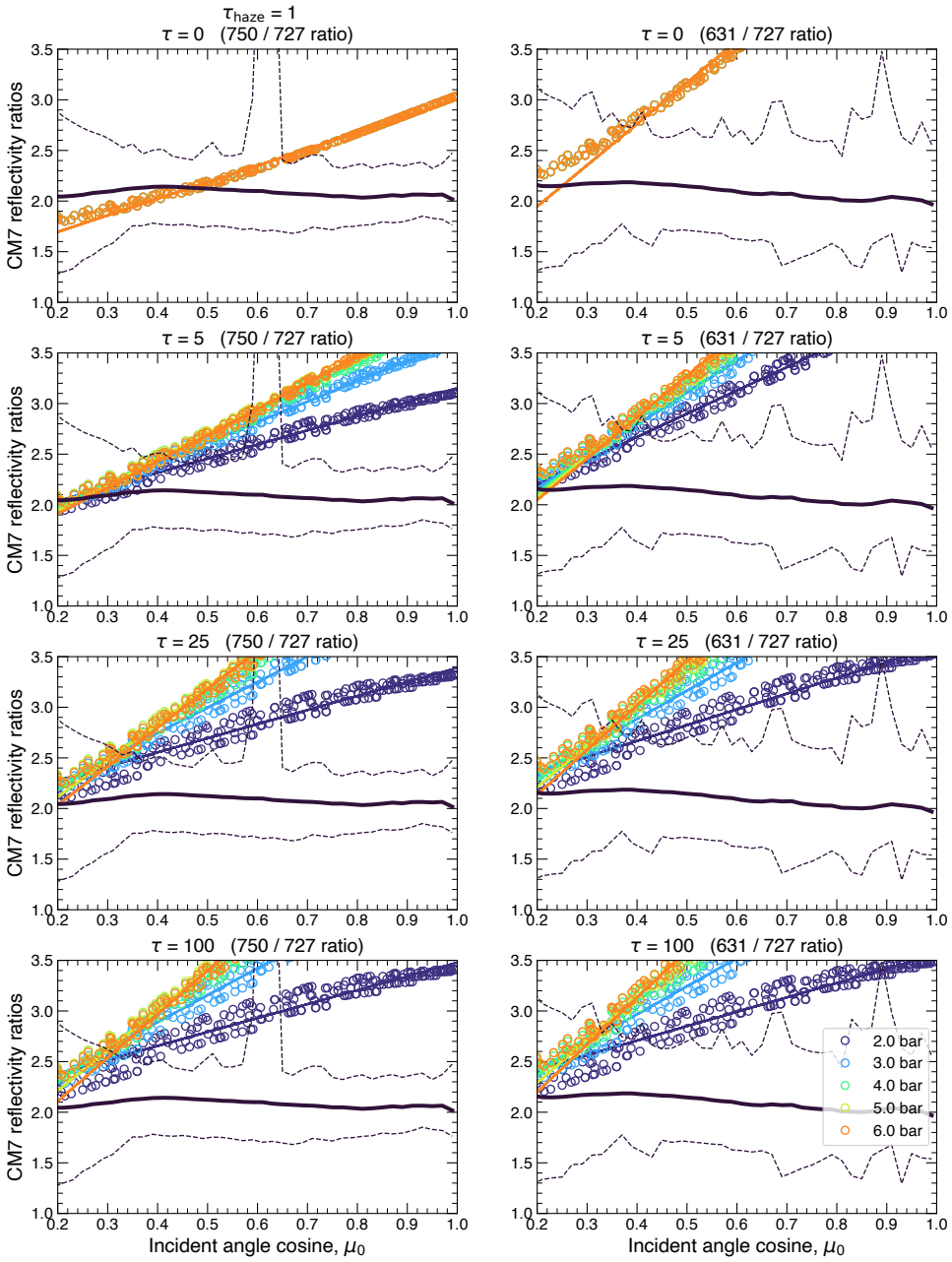

Figure S18. Comparison between observed CM7 and modeled ratios for all model runs with τ_{haze} = 1.

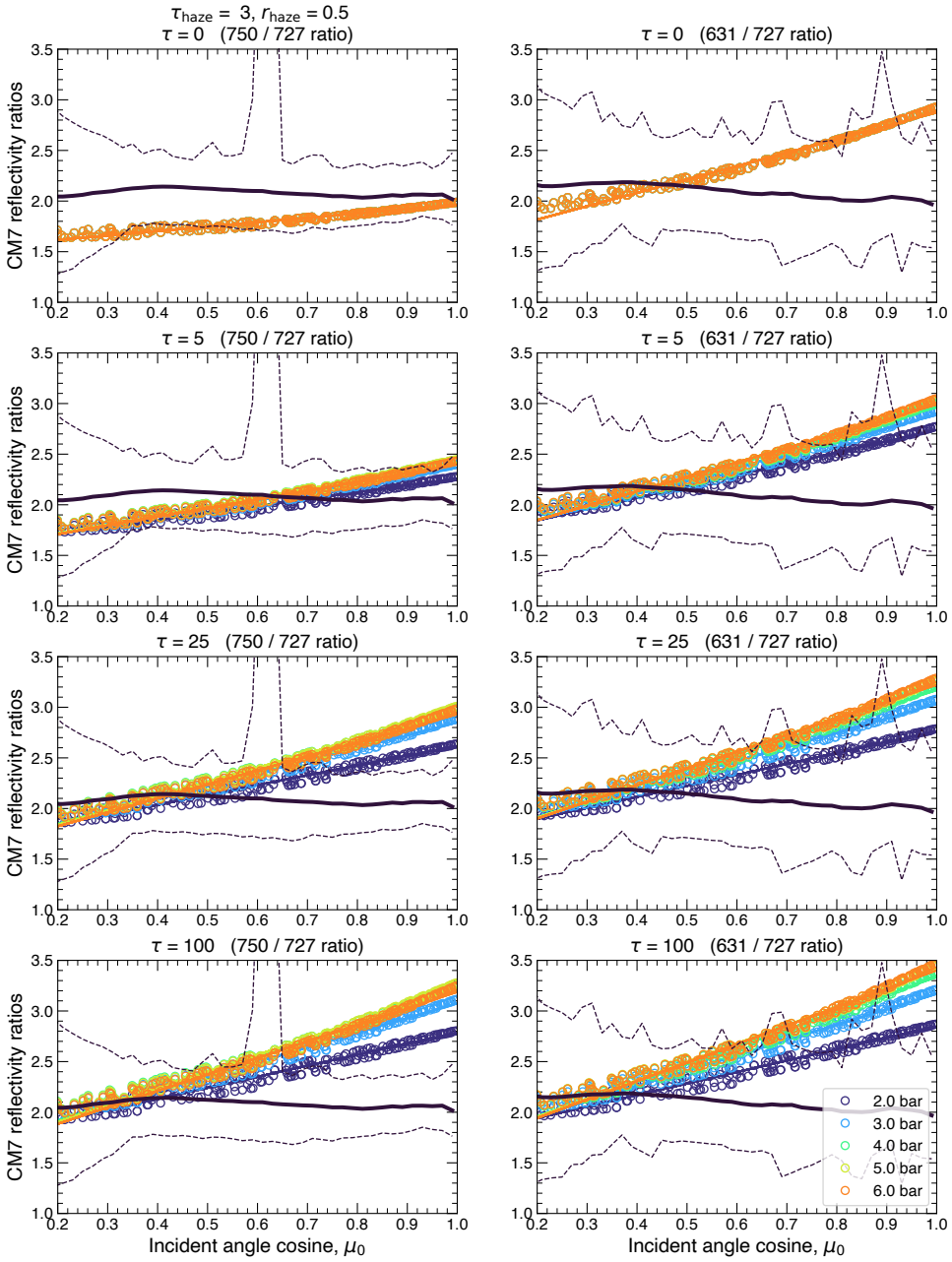

Figure S19. Comparison between observed CM7 and modeled ratios for all model runs with τ_{haze} = 3.

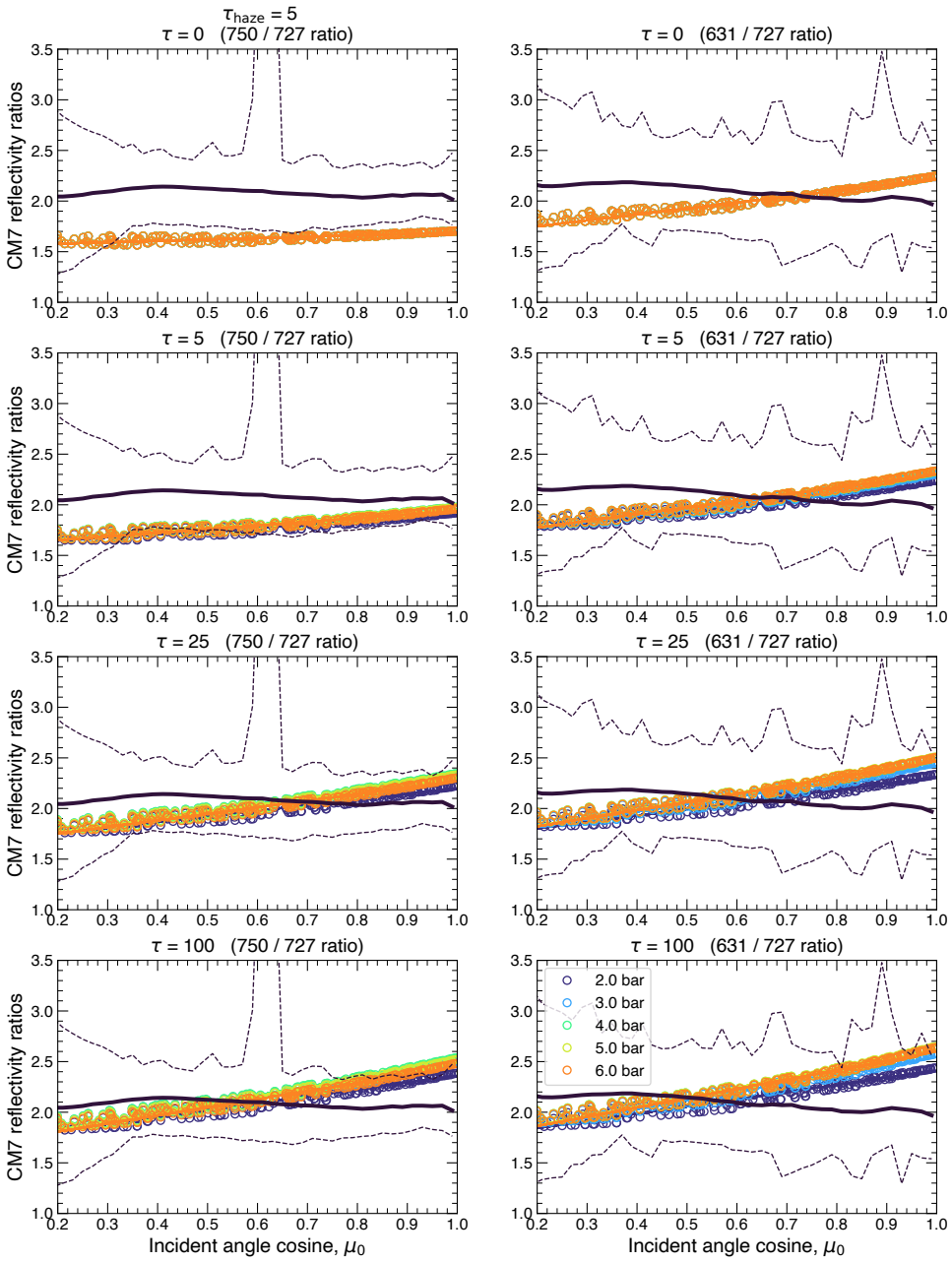

Figure S20. Comparison between observed CM7 and modeled ratios for all model runs with τ_{haze} = 5.

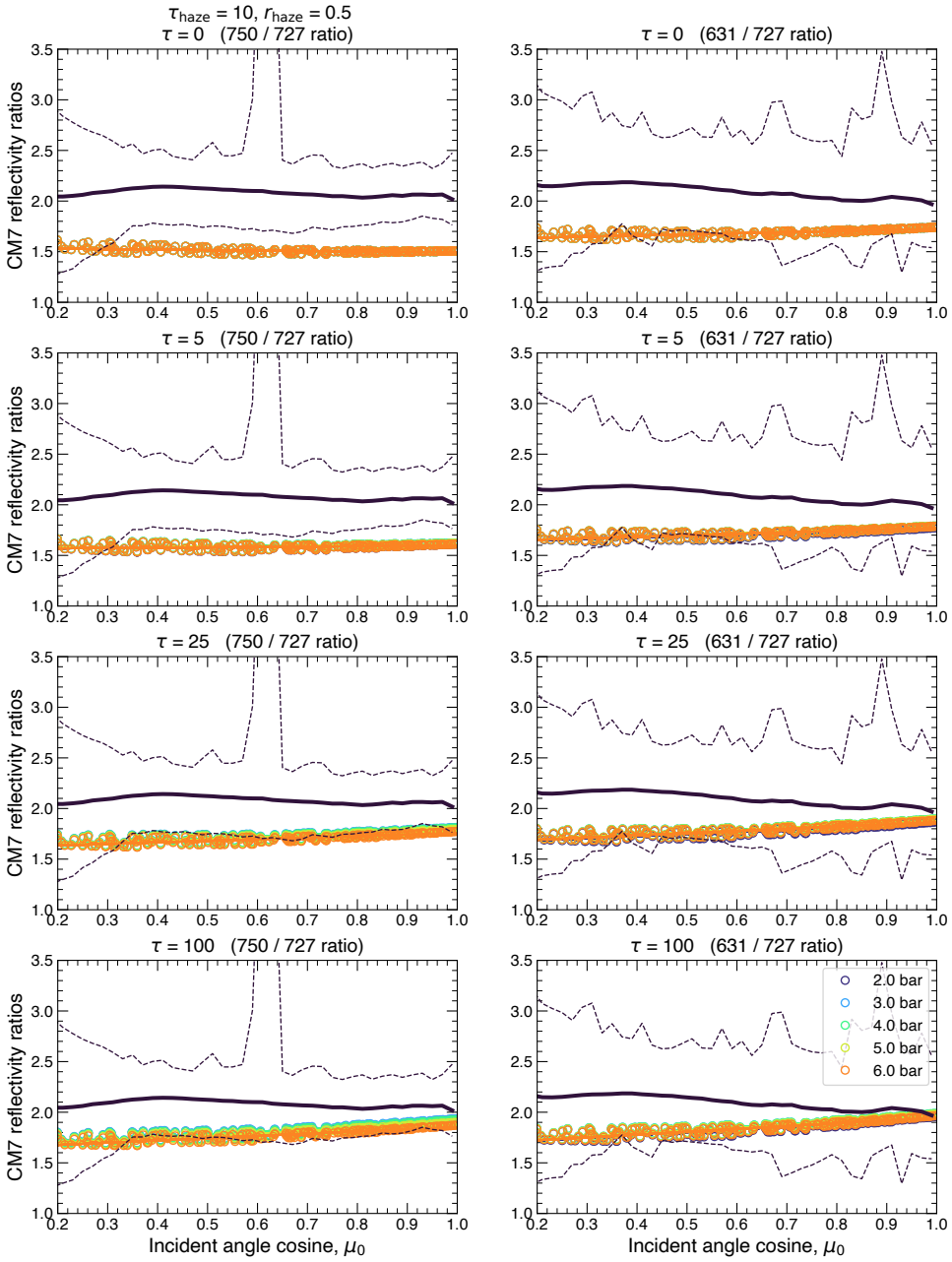

Figure S21. Comparison between observed CM7 and modeled ratios for all model runs with τ_{haze} = 10.

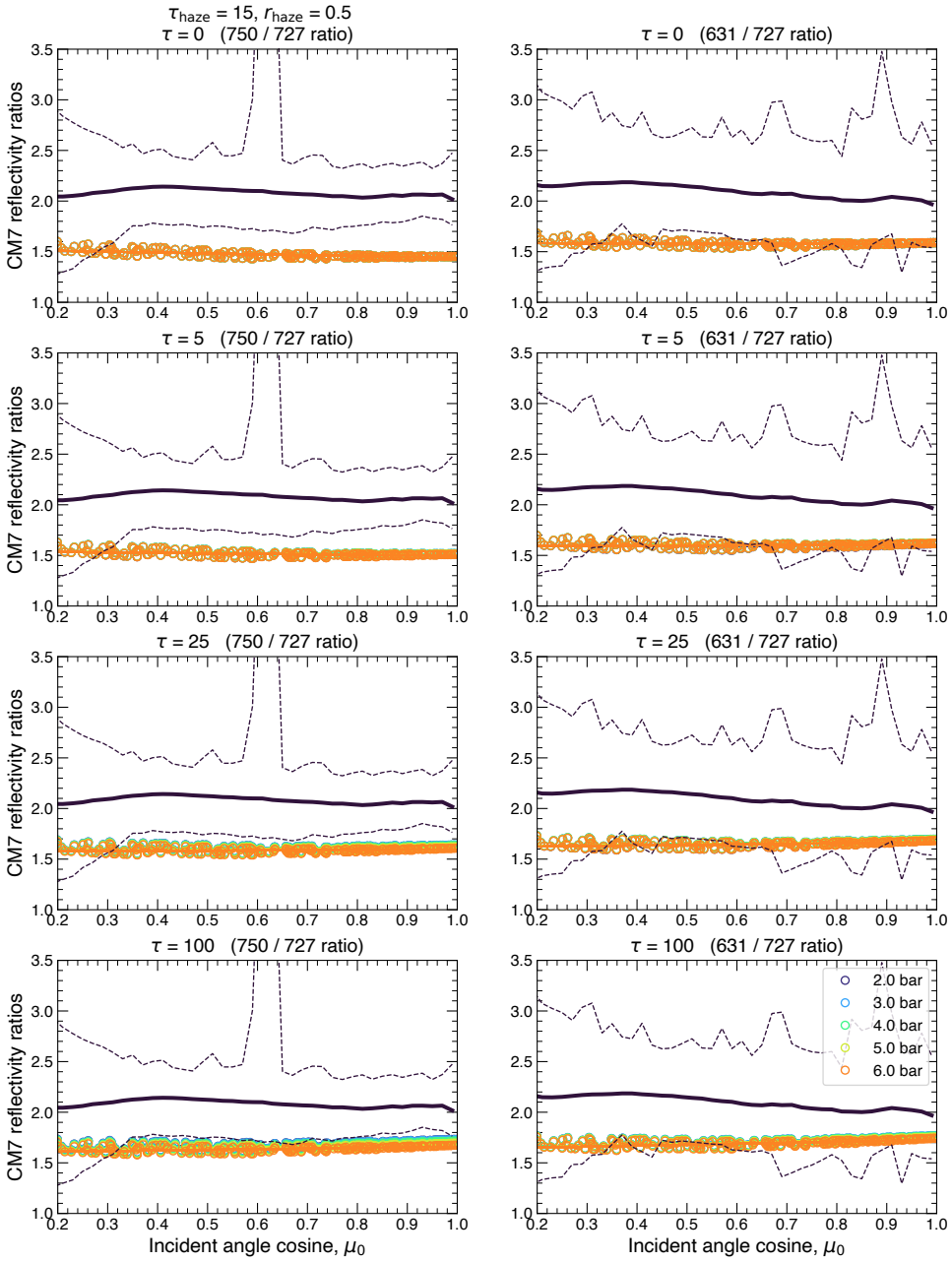

Figure S22. Comparison between observed CM7 and modeled ratios for all model runs with τ_{haze} = 15.